Published in final edited form as:
Mol Cancer Res. 2011 March ; 9(3): 259–270. doi:10.1158/1541-7786.MCR-10-0469.

HIF-1 Dependent Stromal Adaptation to Ischemia Mediates *In Vivo* Tumor Radiation Resistance

David L. Schwartz[*,#], **James Bankson**[o,1], **Luc Bidaut**[o,1], **Yi He**[*], **Ryan Williams**[†], **Robert Lemos**[†], **Arun Thitai-Kumar**[#], **Junghwan Oh**[*], **Andrei Volgin**[#], **Suren Soghomonyan**[#], **Hsin-Hsien Yeh**[#], **Ryuichi Nishii**[#], **Uday Mukhopadhay**[#], **Mian Alauddin**[#], **Ioseb Mushkudiani**[#], **Norihito Kuno**[*], **Sunil Krishnan**[*], **William Bornman**[†], **Stephen Y. Lai**[§], **Garth Powis**[†], **John Hazle**[o,2], and **Juri Gelovani**[#,2]

[*]Department of Radiation Oncology, UT M.D. Anderson Cancer Center, 1515 Holcombe Boulevard, Houston, TX, 77030, U.S.A.

[#]Department of Experimental Diagnostic Imaging, UT M.D. Anderson Cancer Center, 1515 Holcombe Boulevard, Houston, TX, 77030, U.S.A.

[o]Department of Imaging Physics, UT M.D. Anderson Cancer Center, 1515 Holcombe Boulevard, Houston, TX, 77030, U.S.A.

[†]Department of Experimental Therapeutics, UT M.D. Anderson Cancer Center, 1515 Holcombe Boulevard, Houston, TX, 77030, U.S.A.

[§]Department of Head and Neck Surgery, UT M.D. Anderson Cancer Center, 1515 Holcombe Boulevard, Houston, TX, 77030, U.S.A.

Abstract

Purpose—Hypoxia inducible factor (HIF)-1 promotes cancer cell survival and tumor progression. The specific role played by HIF-1 and tumor-stromal interactions towards determining tumor resistance to radiation treatment remains undefined. We applied a multi-modality preclinical imaging platform to mechanistically characterize tumor response to radiation, with a focus on HIF-1 dependent resistance pathways.

Methods—C6 glioma and HN5 human squamous carcinoma cells were stably transfected with a dual HIF-1 signaling reporter construct (dxHRE-tk/eGFP-cmvRed2XPRT). Reporter cells were serially interrogated *in vitro* before and after irradiation as monolayer and multicellular spheroid cultures, and as subcutaneous xenografts in *nu/nu* mice.

Results—*In vitro*, single-dose irradiation of C6 and HN5 reporter cells modestly impacted HIF-1 signaling in normoxic monolayers and inhibited HIF-1 signaling in maturing spheroids. In contrast, irradiation of C6 or HN5 reporter xenografts with 8 Gy *in vivo* elicited marked upregulation of HIF-1 signaling and downstream pro-angiogenic signaling at 48 hours which preceded recovery of tumor growth. *In situ* ultrasound and dynamic contrast enhanced (DCE)-MRI indicated that HIF-1 signaling followed acute disruption of stromal vascular function. High-resolution PET and dual-contrast DCE-MRI imaging of immobilized dorsal skin window tumors confirmed post-radiotherapy HIF-1 signaling to spatio-temporally coincide with impaired stromal

Address for Correspondence: David L. Schwartz, M.D. Department of Radiation Medicine Hofstra North Shore-LIJ School of Medicine 270-05 76th Ave. New Hyde Park, NY 11040 Tel: 516-470-7190 Fax: 516-470-8445 dschwartz3@nshs.edu.
[1]These authors contributed equally.
[2]These authors contributed equally.

Disclosure/Conflict of Interest: N. Kuno is an employee of Hitachi Ltd.

vascular function. Targeted disruption of HIF-1 signaling established this pathway to be a determinant of tumor radioresistance.

Conclusions—Our results illustrate that tumor radioresistance is mediated by a capacity to compensate for stromal vascular disruption through HIF-1 dependent pro-angiogenic signaling, and that clinically relevant vascular imaging techniques can spatially define mechanisms associated with tumor irradiation.

Keywords

Hypoxia; HIF-1; Radiation; Tumor Microenvironment; Imaging; Treatment Response; Stromal Adaptation

INTRODUCTION

Tumor hypoxia predicts for tumor radioresistance and poor clinical outcome (1-3). Tumor cells which survive hypoxic stress are selected for reduced apoptotic potential, increased angiogenic signaling, enhanced metastatic capability, and greater resistance to radiotherapy and cytotoxic chemotherapy. The biological cornerstone of these hypoxia-specific stress responses is the hypoxia-inducible factor 1 (HIF-1) transcription factor (4). Given HIF-1's pro-survival and angiogenic effects, targeted inhibition of HIF-1 signaling has generated interest as a target for therapeutic modulation of radioresistance (5). We have previously confirmed tumor radiosensitization with selective pharmacologic blockade of tumor HIF-1 signaling in glioma, squamous cell, and pancreatic cancer cell lines (6,7). Nonetheless, the temporal dynamics and compartmental sources (e.g. tumor cells versus stromal vessels) of HIF-1 mediated pro-angiogenic responses to radiation have not been elucidated; serial *in situ* imaging would be an ideal means by which to identify such responses to guide future studies to identify optimal timing of HIF-1-targeted intervention with radiation delivery.

Tumor vessels are distinct from their normal counterparts by virtue of their dependence on pro-survival stimulatory cytokines, such as vascular endothelial growth factor (VEGF)(8). Tumor cells upregulate VEGF expression in direct response to irradiation (9), but the relative contribution of direct stimulation of VEGF signaling in tumor cells by radiation versus indirect ischemic HIF-1 stimulation of VEGF expression in tumor cells through radiation-induced disruption of vascular supply is not clear. Recent data (10) suggested that radiation can induce ischemia-reperfusion and reoxygenation-dependent HIF-1 signaling which prompts pro-angiogenic cytokine secretion, enhanced endothelial viability, and improved xenograft survival following irradiation which is sensitive to pharmacologic inhibition of HIF-1. However, the mechanistic interpretation of results from this study remains unconfirmed.

In the current study, we investigated the mechanism and spatio-temporal dynamics of HIF-1 mediated responses to radiation in C6 glioma and HN5 squamous carcinoma HIF-1 reporter cell lines (11,12). In contrast to the reoxygenation-related mechanisms suggested previously, our results indicate that tumor cell HIF-1 signaling is closely associated with microenvironmental ischemia. We first observed in monolayer cultures and multicellular spheroids that radiation minimally impacts or inhibits HIF-1 transcriptional activity. In contrast, *in vivo* irradiation of C6 and HN5 tumor xenografts with 8 Gy led to hypoxia-dependent upregulation of HIF-1 signaling at 48 hours. Immunohistochemical staining and novel high-resolution, HIF-1-specific PET and dual-tracer DCE-MRI imaging of an immobilized dorsal skin window tumor model confirmed that delayed upregulation of HIF-1 signaling and VEGF production in the tumor cell compartment was induced by disruption of stromal vascular function. *In vivo* pharmacologic or genetic knockdown of HIF-1 signaling

suppressed adaptive tumor revascularization and abrogated tumor regrowth following irradiation. These findings establish a foundation for refinement of rationally-designed preclinical HIF-1 targeting strategies, and indicate that clinically available imaging techniques such as DCE-MRI and ultrasound promise immediate relevance towards streamlining translation of these strategies into clinical trials.

METHODS

Reporter Cell Culture and shRNA knockdown

C6 rat glioma cells were obtained from ATCC, while HN5 human squamous cell lines were provided by Dr. Luka Milas (M.D. Anderson Cancer Center, Dept. of Experimental Radiation Oncology). C6 (designated #4C6) and HN5 cells were stably transfected with a dual HIF-1 signaling reporter construct (dxHRE-tk/eGFP-cmvRed2XPRT), which has a bifunctional genetic reporter consisting of herpes simplex virus 1-thymidine kinase (HSV-tk) and green fluorescent protein (GFP) under transcriptional control of the hypoxia response element (12). This construct generated intranuclear GFP signal and HSVtk gancyclovir analog retention under the control of 8x tandem hypoxia response elements. Cytoplasmic RFP signal under CMV promoter control provided baseline beacon signal. For experiments in hypoxic conditions, culture flasks and plates were incubated for noted times and sequences at 37°C in humidified hypoxic air (1% O_2, 5% CO_2, 94% N_2) using an InVivo Hypoxic Workstation 400 with a Ruskin hypoxic gas mixer (Biotrace International, Bridgend, UK). Human HIF-1α shRNA oligonucleotide (ggcttaccatcagctatttctcaagagaaaatagctgatggtaagcctc) was cloned into the pSingle-tTS-shRNA vector (Clontech, Mountain View, CA) at HindIII and XhoI sites. The recombinant vector was transfected using Lipofectamine 2000 per manufacturer's protocol into HN5 HIF-1 reporter cells. Stable, clonal transformants were selected with G418. HN5 reporter cells transfected with pSingle-tTS-scrambled shRNA vector were created as controls.

Monolayer XRT/Treatments/GFP Quantification

Cells were grown on 96-well plates at 1×10^4 cells/well for 24 hours, treated with 0-16 Gy single fraction irradiation per ^{137}Cs unit at 5.8 Gy/min +/− concurrent exposure to 200 μM $CoCl_2$. GFP/RFP signal ratio, to correct inducible GFP signal for baseline reporter activity, was determined by fluorescence spectrometry via an automated TECAN Freedom Evo microplate reader (Durham, NC), and normalized according to viable cell density as quantified by WST1 uptake, as previously described (6).

Spheroid XRT/Treatments/GFP Quantification/Immunohistochemisty

#4C6 multicellular spheroids were generated from 2×10^3 cells in 96-well V-bottomed plates as previously described (12). Individual spheroids were transferred into agarose coated 96-well flat-bottomed plates and were treated with 0-16 Gy single fraction irradiation as described above for monolayer cultures 2 days after plating, +/− concurrent 200 μM $CoCl_2$ treatment. Cell viability confirmation and GFP/RFP signal ratio measurement were also as above. GFP signal was normalized to constitutive RFP signal, and was scaled from a baseline value of 1 at day 0 of each experiment. Digital photomicrographs were taken via a CCD camera-mounted Olympus IX81/FV1000 Fluoview confocal microscope. For immunohistochemical analysis, three spheroids were serially sectioned in their entirety (3-4 adjacent sections, 4 μm thickness) at 50 μm intervals. Immunohistochemical staining, digital microphotography, and image analysis were performed as indicated below for tumor tissue.

Clonogenic Survival Assays

HN5-hre-HIFshRNA cells were grown to 70% confluence with or without treatment with 1 μg/ml doxycycline for 72 hours. During the final 24 hours, cells were incubated at 21% O_2 (normoxia) or 1% O_2 (hypoxia, via chamber) and irradiated with a ^{137}Cs source (5.8 Gy/min), with atmospheric conditions maintained. Cells were assayed for colony formation by replating at specified numbers into 6-well plates in drug-free medium. The cells were immediately plated after irradiation, maintained for 12 days in normoxia, and stained with 0.5% crystal violet in absolute ethanol. Colonies with more than 50 cells were counted. Clonogenic survival curves were constructed from three independent experiments.

In Vivo Limb and Dorsal Tumor Window Xenografts

2×10^6 #4C6 or HN5 reporter cells were implanted subcutaneously into the right forelimb of *nu/nu* mice. Xenografts were allowed to grow to approximately 250 mm^3 over two weeks prior to treatment and imaging. HN5 HIF-1 shRNA knockdown xenografts were implanted in an identical fashion. Tumor volumes were determined from digital caliper measurements using the following formula: tumor volume (cubic millimeters) = $\pi/6$ [(short axis in mm)^2 * (long axis in mm)]. For the dorsal tumor window tumor model, MRI-compatible Duralon dorsal flank skin windows were secured with non-absorbable suture, and 2×10^5 #4C6 reporter cells were injected subcutaneously within the window. Tumors grew for approximately 12 days to a volume of 150 mm^3 prior to treatment and imaging. All animals were handled and treated according to Institutional Animal Care and Utilization Committee guidelines.

Animal Irradiation

Irradiated tumors received 8 Gy single fraction treatment via a ^{60}Co unit at 1.8 Gy/min with custom head and body shielding.

Tumor Tissue Immunohistochemistry and Image Analysis

Control and radiated tumors were collected at indicated timepoints. Pimonidazole was injected IV into animals 60 minutes prior to sacrifice at a concentration of 25mg/ml. Tumors were routinely fixed in 4% formaldehyde/PBS and processed into paraffin, and then sectioned at 4 μm thickness. To ensure adequate sampling, four tumors for each treatment condition were collected, bi-sected, and then serially sectioned (10 adjacent sections, 4 μm thickness) at 100-150 μm intervals in either direction. Immunohistochemical staining for individual epitopes was performed on a Vision Biosystems Bondmax automated slide stainer (VBS, Norwell, MA) and nuclei were visualized by staining with hematoxylin. Pimonidazole adducts were stained using a FITC-labeled monoclonal antibody, followed by an HRP-conjugated anti-FITC polyclonal antibody (Hypoxyprobe-1 Plus, Chemicon, Temecula, CA). Tumor vasculature was visualized with a polyclonal CD105 antibody (R&D Systems, Minneapolis, MN). HIF-1α was detected by monoclonal antibody from BD Transduction Laboratories (Lexington, KY), Ki-67 and GFP were detected by polyclonal antibodies from Abcam (Cambridge, MA), while VEGF and cleaved caspase-3 were detected by polyclonal antibodies from R&D Systems (Minneapolis, MN), and Cell Signaling (Boston, MA), respectively. Specificity of all staining was confirmed with non-specific control antibodies. High-resolution images were acquired using a Nikon e90i microscope with automated stage and a Roper Coolsnap K4 digital camera (Roper Scientific, Tucson, AZ) through a plan-apo 4x objective. Sections were imaged in their entirety, manually registered with Photoshop CS2 software to permit direct overlay with staining from adjacent slices, and analyzed on a pixel-by-pixel basis for signal intensity and overlap using Compix SimplePCI (Hamamatsu Corp, Bridgewater, NJ) image analysis software. Intensity cutoffs were empirically determined for each antigen based on the

control non-specific antibody slides and used for every image from that antibody series. Percent pixel-to-pixel GFP and VEGF signal overlap with pimonidazole was quantified as (100)(# GFP-VEGF and Pimo positive pixels)/(total # GFP-VEGF positive pixels) was quantified for all analyzed sections and pooled for statistical analysis.

MicroPET Whole Animal Imaging

Repetitive, non-invasive whole animal molecular-genetic PET imaging of HIF-1 signaling was made possible through selective intracellular retention of radiolabeled reporter substrate 2′-^{18}F-fluoro-2′-deoxy-5-ethyl-1-β-D-arabionofuranosyluracil (^{18}F-FEAU). ^{18}F-FEAU was synthesized using a modified no-carrier added procedure (13). For each time point and study condition, 9-10 mice were injected (i.v.) with 100 μCi (100 μL) of ^{18}F-FEAU. Fifteen-minute static images were acquired under inhalation anesthesia on a commercial microPET system (Concorde Microsystems, R4, Knoxville, TN). Images were reconstructed by using ordered subset expectation maximization (OSEM) algorithm. Regional radioactivity concentrations (KBq/cm^3 or μCi/cm^3) for ^{18}F-FEAU was estimated from regions of interest (ROIs) drawn around the tumor or organ on trans-axial slices from the reconstructed image sets. Tumor tracer uptake was normalized to background muscle uptake in the contralateral shoulder and quantified as a maximal tumor to muscle ratio (TMR) averaged from three separate levels on axial projection, measured in triplicate with standardized 3-7 pixel diameter 2D regions of interest. Pooled results from each study animal group were reported as mean values +/− standard error.

Ultrasound Imaging

Ultrasound imaging of xenografts was performed with a Vevo 770 system (VisualSonics, Toronto, ON), using a single-element transducer with 40 MHz center frequency. Power Doppler settings were held constant at 25dB Power Doppler gain, 5 KHz pulse repetition rate, 2.5mm/s wall filter with 2mm/s scan speed. Initial imaging of tumor was performed in B-mode to discriminate tumor boundaries, and Doppler images were acquired for a manually delineated region of interest encompassing the entire tumor. Vascular area in tumor was calculated by color pixel density (CPD), defined as the ratio of the number of color pixels (i.e., pixels with a Doppler measurable flow) to the total number of pixels within the region of interest.

MRI Imaging

Serial single-tracer dynamic, contrast-enhanced (DCE)-MRI data from a six mouse xenograft study cohort treated with 8 Gy single dose irradiation was acquired using a 4.7T Biospec USR47/40 small animal imaging system (Bruker Biospin MRI, Inc., Billerica, MA) with a 35-mm linear volume resonator and 60-mm micro-imaging gradients. A three-plane RARE imaging sequence was used to confirm animal positioning, and coronal T_2-weighted RARE images (TE/TR 70/4000ms, FOV 4cm × 3cm, matrix 256 × 192, RARE factor 12) were used for tumor localization. Axial T_1-weighted spin-echo images (TE/TR 8.5ms/700ms, FOV 4cm × 3cm, matrix 256 × 192) were acquired before and after administration of 0.2 mmol/kg gadopentetate dimeglumine (Gd-DTPA: Magnevist, Berlex Laboratories, Montville, NJ), an FDA-approved T_1-reducing contrast agent. DCE-MRI data was acquired using a multi-slice fast spoiled gradient-recalled echo sequence (TE/TR 1.4/40ms, FOV 4cm × 3cm, matrix 128 × 96, 35° excitation angle, 3.8 sec/repetition, 100 repetitions). Baseline images were collected for one minute prior to injection of the contrast agent. A generalized kinetic model (14,15) was applied to manually segmented data using Matlab (The Mathworks, Natick, MA).

Dorsal Skin Window Tumor Imaging

Mice were immobilized under inhalation anesthesia on a CT/MRI/PET/ultrasound-compatible sled with a built-in MR surface coil and ^{68}Ge point-source fiducial markers adjacent to window frames for *post-hoc* image localization and registration. Fluctuations in signal relaxation (T_2*) due to susceptibility differences (often attributed to changes in oxygen saturation) were measured using a multi-echo gradient-echo sequence (TE_{min} 4.5ms, 7.23ms interval between each of 12 echoes, TR 1500ms, FOV 2cm × 1.5cm, matrix 256 × 256). A dual-tracer DCE-MRI acquisition (16) was employed using PG-Gd-DTPA (17) and Magnevist. After 1 minute of T_1-weighted baseline scans using a fast spoiled gradient-echo sequence (TE/TR 1.65ms/75ms, FOV 2cm × 1.5cm, matrix 128 × 96, 50° excitation angle), 0.06 mmol/kg PG-Gd-DTPA was injected via tail vein catheter. Five minutes later, 0.2 mmol/kg Magnevist was injected, and enhancement was monitored for three more minutes. All data was segmented manually and analyzed using Matlab. HIF-1 signaling detection with ^{18}F-FEAU-PET was performed as above. To facilitate registration, 3D microCT imaging was obtained with an eXplore micro-CT system (GE Healthcare, Buckinghamshire, UK). All imaging was completed within 4 hours. PET was first registered to the reference anatomical CT through a gross rigid transformation to match marker sets and major structures such as body outlines that are visible on both modalities. This initial registration was then further refined through the multi-resolution iterative maximization of a normalized mutual information (NMI) cost function (18). A similar process was used to register MR to CT, albeit with a high resolution field of view that was limited to anatomy that was visible within the physical tumor window. Once registered together, the PET, CT and MR data sets were fused together, processed and visualized (19) to localize and compare PET uptakes and MR parametric maps in relation to structural anatomy.

Statistical Testing

Significance of difference between pooled results from study groups was measured via unpaired two-sided Student *t*-testing using GraphPad v.4 (San Diego, CA).

RESULTS

In situ functional imaging demonstrates tumor cell HIF-1 radiation response to be unique to the *in vivo* setting

Radiation minimally impacted or inhibited tumor cell HIF-1 signaling in the absence of vascularized stroma. There was no change in HIF-1 dependent GFP signal in normoxic #4C6 and HN5 HIF-1 reporter monolayers following escalating doses up to 8 Gy, although a decrease in HIF-1 signal was seen uniquely in #4C6 cells 72 hours following 16 Gy (Figure 1a). Irradiation of chemically hypoxic (200 μM $CoCl_2$) cells with up to 16 Gy did not alter HIF-1 activity, indicating that radiation does not directly impact ongoing tumor HIF-1 signaling response to hypoxic stress (Figure 1b). Radiation treatment *in vitro* modestly impacted downstream VEGF signaling in the absence of upstream HIF-1 induction. VEGF mRNA remained stable and soluble protein expression increased incrementally in normoxic #4C6 or HN5 monolayers treated with 8 Gy (data not shown). Hypoxic #4C6 or HN5 monolayers demonstrated an expected increase in VEGF protein expression within 48 hours, which was unaffected by 8 Gy treatment, consistent with HIF-1 expression results.

To further model the microenvironment of hypoxic tumors, #4C6 cells were cultured as three-dimensional spheroids measuring at least 500 μm in diameter. Confocal microscopy revealed hypoxia/HIF-1 induced GFP signal in the central region of spheroids extending outward to a depth of approximately 100 μm from the surface. Single fraction irradiation inhibited GFP expression in maturing spheroids in a dose-dependent manner (Figures 1c-d). Quantified immunohistochemical staining of spheroids confirmed reduction of centralized

HIF-1 and downstream VEGF signal in spheroids treated with 4-8 Gy (Figure 1e). Treatment with up to 16 Gy did not inhibit pre-existing HIF-1 signaling or VEGF expression in spheroids treated with 200 μM $CoCl_2$ (Figure 1c).

Although direct effects of radiation on tumor cell HIF-1 signaling appeared modest, we observed profound HIF-1 tumor cell signaling responses within intact vascularized tumors. *Nu/nu* mice ($n = 9$) bearing #4C6 xenografts were serially imaged for HIF-1 transcriptional activity with ^{18}F-FEAU-PET over 8 days. Treatment with 8 Gy induced delayed, incremental upregulation of HIF-1 activity in tumor cells at 48 hours (mean maximum tumor-muscle activity ratio [TMR] of ^{18}F-FEAU accumulation = 4.51 +/− 0.23 standard error versus 3.97 +/− 0.11 for controls, $p < 0.05$; Student's *t* test) which subsequently peaked at Day 6 post-treatment (mean maximum TMR = 7.85 +/− 0.24 versus 5.77 +/− 0.18 for controls, $p < 0.005$). HIF-1 upregulation was heterogeneous and discretely localized to viable peripheral regions within tumors (Figure 2a). The marked upregulation of HIF-1 activity observed in irradiated tumors at Day 6 subsequently decreased by Day 8 to levels comparable to controls (mean maximum TMR = 5.64 +/− 0.22 versus 5.21 +/− 0.17 for controls, p = n.s.). HIF-1 upregulation in irradiated tumors was accompanied by refractory, albeit slowed, tumor growth (Figure 2b). ^{18}F-FEAU-PET imaging of irradiated HN5 reporter xenografts ($n = 6$) confirmed similar findings (Figure 2b).

Stromal vessel dysfunction and ischemic insult are closely associated with post-radiation HIF-1 tumor cell signaling

We interrogated temporal kinetics and spatial associations between post-radiation microenvironmental stress and tumor cell HIF-1 signaling in greater detail by immunohistochemical staining. #4C6 tumors treated with 8 Gy demonstrated an acute reduction in overall tumor HIF-1 dependent GFP reporter and VEGF expression at 4 hours (Figure 3). A concomitant decrease in pimonidazole staining demonstrated that, at this stage, tumors were less hypoxic. This was associated with metabolic and proliferative arrest in tumor cells rather than improved tumor perfusion, as evidenced by reduced ^{18}F-FDG uptake, BrdU and Ki-67 tumor proliferation indices, and ^{18}F-2′-deoxy-2′-flouro-5-methyl-1-beta-D-arabinofuranosyluracil (FMAU) proliferation tracer uptake at 24 hours post-radiation (data not shown). However, localized, discrete areas of persistent HIF-1 dependent GFP signaling and VEGF signal were observed, closely correlating with areas with pimonidazole retention (Figure 3a). Quantitative pixel-by-pixel analysis of GFP and VEGF IHC images co-registered with pimonidazole IHC images confirmed that high baseline spatial overlap of GFP (44.84% ± 11.85%) and VEGF (38.85% ± 11.15%) signal with regions of physical hypoxia remained unchanged 48 hours following radiation treatment (43.68% ± 11.18% for GFP and 34.60% ± 8.84% for VEGF, p = ns, Figure 3c), arguing against a functional association between reoxygenation events and HIF-1 signaling. Vascular endothelial cells positive for both for CD105 and cleaved caspase 3 were seen exclusively in regions devoid of GFP and VEGF signal.

In situ ultrasound and DCE-MRI imaging of irradiated #4C6 xenografts functionally corroborated these findings. Eight Gy treatment led to transient disruption of tumor blood flow on power Doppler ultrasound ($n = 6$ per cohort). This was observed within 24 hours following completion of radiation (74.9% +/− 1.1 % decrease, $p < 0.001$), with a notable loss of blood flow within the central and superficial portions of xenografts away from extrinsic host soft tissues (Figure 4a). This reduced blood flow was accompanied by an increase in globally quantified measures of vascular permeability, demonstrated by increased average K^{trans} (min^{-1}, a rate constant which is potentially value-limited by either blood flow or vessel permeability) values from single-tracer DCE-MRI mapping (578% +/− 57% increase, $p < 0.005$) within 24 hours (Figure 4b). Acutely increased K^{trans} values were distributed heterogeneously within non-necrotic regions, consistent with regionalized loss of

vascular integrity and blood flow within remaining functional stroma. Both blood flow and K^{trans} values began to return towards baseline at 48 hours, in concert with the timing of HIF-1 upregulation.

High-resolution multi-modality imaging localizes post-radiation HIF-1 signaling to regions of impaired vascular function

We employed co-registered PET, dual high/low molecular weight tracer DCE-MRI, MR angiography, and MR relaxometry in a dorsal skin window tumor system to co-localize post-radiation HIF-1 tumor signaling to regions of stromal dysfunction and low oxygen tension. Fiducial landmarks and mechanical immobilization provided by the dorsal skin window frame permitted high-fidelity image co-registration. Dual-tracer DCE-MRI provided reproducible estimation of vessel permeability in the absence of vascular input data from major vessels within the field-of-view of the surface coil. PET imaging of #4C6 skin window tumors (n = 6) reproduced earlier findings of tumor HIF-1 signaling 2 days post-radiation. Overlap between HIF-1 dependent ^{18}F-FEAU signal and low molecular weight contrast delivery to the extravascular compartment (Figure 5) confirmed close co-localization of HIF-1 signaling with post-radiation tumor microvessel disruption. The timing and location of these imaging biomarkers corroborate a direct functional association between adaptive HIF-1 tumor cell signaling and abrupt ischemic microenvironmental stress following irradiation.

Post-radiation HIF-1 tumor cell signaling precedes tumor stromal recovery and is a necessary determinant of tumor radiation resistance

Consistent with our imaging results, immunohistochemical staining confirmed regionalized ischemic upregulation of HIF-1 transcriptional activity and VEGF expression 36 to 48 hours following irradiation, most notably in previously perfused peripheral tumor regions (Figure 3a-b). Upregulation of HIF-1 and VEGF signaling was accompanied by the reemergence of a proliferating Ki-67+ tumor cell subpopulation. By one week post-irradiation, CD105+ vessels returned to regions of reduced HIF-1 and VEGF signaling, consistent with physiologically relevant reperfusion. Vascular function returned towards baseline on power Doppler and DCE-MRI by day 7 post-treatment (Figures 4a-b).

Taken together, these findings indicate that ischemia-driven stromal responses are critical to tumor radiation resistance, and provide a mechanistic rationale for targeted disruption of HIF-1. We have previously confirmed tumor radiosensitization with targeted pharmacologic blockade of tumor HIF-1 signaling with the selective HIF-1 inhibitor PX-478 in C6, HN5, and pancreatic cancer cell lines (6,7). Power Doppler and DCE-MRI demonstrated that PX-478 abolishes HIF-1 dependent post-radiotherapy tumor stromal recovery, and that constitutive expression of downstream angiogenic signals can restore refractory tumor vessel function during drug exposure. To confirm specificity of these findings, we introduced conditionally inducible human HIF-1 shRNA into HN5 reporter cells, which yielded inhibition of HIF-1 and downstream VEGF expression in response to hypoxic stimulation (1% O_2 for 24 hours) (Figure 6a-b). HIF-1 shRNA induction yielded a modest direct effect on hypoxic cells, with a sensitizer enhancement ratio at 0.2 surviving fraction of 1.35 vs. 1.01 seen in 1% and 21% O_2 conditions, respectively (Figure 6c). Induction of HIF-1 shRNA *in vivo* in HN5 xenografts inhibited HIF-1 expression detected by IHC/Western blotting as well as downstream HIF-1 signal detected by GFP expression (not shown). Identical to PX-478, induction of HIF-1 shRNA (5 mg doxycycline via oral gavage x 3 days) prior to 8 Gy irradiation of HN5 xenografts led to stable tumor growth delay not seen following either treatment alone (Figure 6d).

DISCUSSION

Hypoxia is associated with tumor radiation resistance (3,20-22), and is classically described as a modifier of the physical effects of radiation on tumor cell DNA integrity. *In vitro*, oxygen enhances direct tumor cell killing at clinically relevant radiation doses (23). The degree of hypoxia required to fully demonstrate this phenomenon must be severe (e.g. <5 mmHg oxygen) (24). Adaptive HIF-1 signaling to hypoxia is elicited at much higher concentrations of oxygen (as high as 40 mmHg), with additional modulation occurring as oxygen deprivation becomes more pronounced (25). This underscores a more complicated interaction between hypoxia and tumor cell radiation response in whole tumors, where radiation impacts tumor cell survival both directly and indirectly through effects on stromal cell populations. Tumor cells which successfully adapt to microenvironmental stress are able to co-opt and/or induce stromal blood vessels to enhance their oxygen and nutrient supply by paracrine growth factor signaling (26). HIF-1 stimulated tumor expression of VEGF and other pro-angiogenic factors is key to this process (27). Given that radiotherapy can damage tumor vascular function and lead to secondary ischemic tumor stress, it is logical to expect tumor cell HIF-1 signaling to serve as an important determinant of whole tumor radiation response. This indeed has been shown (10), although the exact mechanisms responsible for post-radiotherapy HIF-1 signaling remain incompletely defined.

Mixed findings have been elicited from *in vitro* studies of HIF-1 tumor cell signaling following radiation (10,28). Using our functional reporter system, we demonstrated tumor HIF-1 signaling responses to irradiation occur exclusively in intact vascularized tumors. Previous data (10) suggest that reoxygenation events are responsible for induction of HIF-1 after irradiation, a phenomenon we did not observe *in vivo*. We directly associated post-radiation HIF-1 upregulation with ischemic microenvironmental stress via submicron-resolution, quantitative analysis of IHC images and non-disruptive, submillimeter-resolution multimodality imaging. Thus, our findings implicate an alternative pathophysiologic cascade in which tumor radioresponse and resistance is determined by ischemic tumor cell maintenance of underlying stromal vascular supply. Although physical hypoxia may directly impart tumor cell radioresistance (e.g. reduced concentrations of free radical species), our results demonstrate that hypoxia can also impact *in vivo* radioresistance through indirect paracrine mechanisms of stromal vascular maintenance. Absence of supportive paracrine tumor cell signaling during irradiation (such as in normoxic tumor regions) would leave endothelial cells more susceptible to dysfunction and killing from radiation. Thus, in C6 and HN5 tumors, chronically hypoxic, yet viable tumor regions contain foci of resistant tumor vessels which themselves serve as the target for post-radiation paracrine signaling from surviving tumor cells, leading to stromal revascularization.

Our results do not exclude re-oxygenation dependent tumor HIF-1 upregulation events following irradiation, particularly in alternative tumor models with less pronounced baseline VEGF signaling than C6 and HN5. In fact, both reoxygenation and ischemic events could conceivably play complementary roles in tumor adaptation and resistance. However, exact delineation of the respective importance of either mechanism across specific tumor types will have key therapeutic implications, since *early* concurrent HIF-1 inhibition would be expected to optimally treat resistant ischemic tumor regions with chronic tumor HIF-1 signaling. Alternatively, sequencing of HIF-1 blockade *after* radiation would potentially best impact tumors relying upon post-treatment reoxygenation to drive adaptive HIF-1 signaling; in fact, data from 4T1 and HCT-116 tumor models directly supports this premise (29).

High resolution small animal imaging is well suited to serially interrogate these mechanisms within intact tumor models. DCE-MRI can quantifiably evaluate integrity and function of tumor microvasculature, as well as tumor response to anti-angiogenic or anti-vascular

therapy (30). The dual-tracer DCE-MRI technique we employed differentiates vascular enhancement from rapid extravasation and correlates better with histologic endpoints than traditional single-tracer studies (16,31). Preclinical ultrasound provides additional quantification of tumor blood flow (32-35). Sophisticated multi-modality approaches are required to capitalize on the complementary strengths of such techniques. Pilot reports have demonstrated the feasibility of combined ultrasound and MRI to assess tumor vessel radiation responses in mouse xenografts (32,33). Other studies have combined vascular MRI imaging with optical assessment of HIF-1 pathway signaling (36) or with pulsed electron paramagnetic resonance (EPRI) localization of physical hypoxia (37). For this study, we leveraged a multi-modality platform utilizing physically immobilized dorsal skin window tumors to obtain high-resolution data with rigorous image co-registration during an extended time course of repetitive imaging. Our studies confirmed expected limitations of this system caused by the discrepancy between MR image resolution (~156 um in-plane) and the point-spread function of PET (~3 mm). Quantification of baseline voxel-to-voxel correlation of PET signal to T_2*/R_2* maps remain difficult to reproduce due to PET resolution limitations, as well as adjacent air-tissue interfaces and tissue heterogeneity. Efforts to improve robustness of quantification are ongoing. Nonetheless, strong qualitative agreement between PET signal and DCE-MRI parametric maps of low molecular weight MR contrast delivery to the extravascular compartment (e.g. Magnevist-dependent permeability maps, Figure 5) confirmed close spatial association of HIF-1 signaling with post-radiation tumor microvessel disruption. Importantly, the lack of correspondence between HIF-1 PET signal and the fraction of tissue volume occupied by vessels (e.g. high molecular weight PG-Gd-DTPA contrast-dependent vascular volume fraction maps, Figure 5) emphasizes the limitations of simple quantified measures of tumor blood vessel density devoid of spatial information.

Targeted inhibition of HIF-1 has been shown to provide direct anti-tumor activity (38) and to enhance tumor radiosensitivity (6,7,39,40) in preclinical studies. Selective HIF-1 pharmacologic inhibitors are now entering early clinical development (41,42). Many questions remain before rationally-designed HIF-1 targeted radiosensitization strategies can be optimized for the clinic. HIF-1 knockdown leads to variable effects across cell types, and may provide ineffective tumor radiosensitization, or even tumor cell radioprotection. The exact cell population which serves as the functional target of HIF-1 inhibition *in vivo* is not certain. This undoubtedly varies across tumor types and disease sites and may, in fact, be stromal constituents (e.g. tumor vessel endothelium) rather than tumor cells themselves. A genetic loss-of-function study with HIF-1α null endothelial cells demonstrated a HIF-1 driven VEGF-VEGFR2 autocrine loop originating within the endothelium which is required for solid tumor angiogenesis (43), supporting the notion that stromal vasculature could be exploited as a direct target of HIF-1 inhibition. Stromal sensitivity to radiation potentially varies across organ sites, not only due to differences in native radioresistance of EC cells, but also the quality, dynamics, and specific signaling proteins responsible for supportive paracrine signaling (44). Blouw, *et al* (45) have demonstrated that HIF blockade can lead to increased vessel cooption and tumor cell invasion in vessel-rich brain parenchyma versus less vascularized subcutaneous tissues, further emphasizing critical tissue-specific effects of HIF-1 blockade. Finally, the respective roles played by different members of the HIF-α family, including HIF-2α and HIF-3α, across individual tumor types remains unclear. Despite similarities between HIF-1α and HIF-2α, there is little redundancy between the downstream effects of these two proteins (46,47). Nonetheless, we have found HIF-2 to be only weakly expressed in C6 and HN5 xenografts (<10% expression by IHC at baseline and post-radiation; data not shown), supporting the primacy of HIF-1-specific adaptive signaling in these models.

CONCLUSIONS

Our results demonstrate a stroma-dependent cascade responsible for whole tumor radioresistance. Radiosensitivity and kinetics of post-radiation vascular recovery depend upon HIF-1-mediated paracrine pro-survival signaling from nutrient-deprived, hypoxic tumor cells to stromal vasculature. Poorly perfused regions in which tumor cells produce higher levels of pro-angiogenic factors selectively protect neighboring microvessels from radiation insult. Tumor regions with normal perfusion and lower levels of pro-angiogenic factors are more sensitive to radiation-induced vascular dysfunction. The degree of ischemic HIF-1 signal stimulation determines the magnitude of adaptive pro-angiogenic signaling from tumor cells to regain stromal support. Therefore, targeted HIF-1 blockade promises effective inhibition of the signaling source for whole tumor adaptation events. *In situ* spatiotemporal imaging promises to clarify the respective roles of constituent tumor subpopulations as well as the temporal dynamics of adaptive post-radiation responses. This information can potentially guide rational administration of targeted radiosensitizing agents, and streamline downstream deployment of such strategies into the clinical trial setting.

Acknowledgments

We acknowledge the expertise and assistance of Drs. Benjamin Moeller and Dominique Jennings with MRI-compatible dorsal skin window platform development. The work was supported by the Experimental Cancer Imaging Research Program (U24-CA126577), NIH grants CA017094 to G. Powis and D. Schwartz, NIH grants CA095060, CA098920, CA1019552 to G. Powis, New Program Development Funds and faculty start-up funding from the Department of Experimental Diagnostic Imaging to J. Gelovani and M. Alauddin, and the Cancer Center Support Grant (P30-CA016672) at M.D. Anderson. D. Schwartz received support from the University of Texas Inter-Institutional Biomedical Engineering Program, and grant-in-aid funding from Hitachi Ltd.

REFERENCES

1. Brizel DM, Scully SP, Harrelson JM, et al. Tumor oxygenation predicts for the likelihood of distant metastases in human soft tissue sarcoma. Cancer Res. 1996; 56(5):941–3. [PubMed: 8640781]
2. Hockel M, Schlenger K, Aral B, Mitze M, Schaffer U, Vaupel P. Association between tumor hypoxia and malignant progression in advanced cancer of the uterine cervix. Cancer Res. 1996; 56(19):4509–15. [PubMed: 8813149]
3. Nordsmark M, Overgaard J. A confirmatory prognostic study on oxygenation status and loco-regional control in advanced head and neck squamous cell carcinoma treated by radiation therapy. Radiother Oncol. 2000; 57(1):39–43. [PubMed: 11033187]
4. Semenza GL. HIF-1: mediator of physiological and pathophysiological responses to hypoxia. J Appl Physiol. 2000; 88(4):1474–80. [PubMed: 10749844]
5. Semenza GL. Targeting HIF-1 for cancer therapy. Nat Rev Cancer. 2003; 3(10):721–32. [PubMed: 13130303]
6. Schwartz DL, Powis G, Thitai-Kumar A, et al. The selective hypoxia inducible factor-1 inhibitor PX-478 provides in vivo radiosensitization through tumor stromal effects. Mol Cancer Ther. 2009; 8(4):947–58. [PubMed: 19372568]
7. Schwartz DL, Bankson JA, Lemos R Jr. et al. Radiosensitization and stromal imaging response correlates for the HIF-1 inhibitor PX-478 given with or without chemotherapy in pancreatic cancer. Mol Cancer Ther. 2010; 9(7):2057–67. [PubMed: 20587661]
8. Carmeliet P. Angiogenesis in life, disease and medicine. Nature. 2005; 438(7070):932–6. [PubMed: 16355210]
9. Kakeji Y, Maehara Y, Ikebe M, Teicher BA. Dynamics of tumor oxygenation, CD31 staining and transforming growth factor-beta levels after treatment with radiation or cyclophosphamide in the rat 13762 mammary carcinoma. Int J Radiat Oncol Biol Phys. 1997; 37(5):1115–23. [PubMed: 9169821]

10. Moeller BJ, Cao Y, Li CY, Dewhirst MW. Radiation activates HIF-1 to regulate vascular radiosensitivity in tumors: role of reoxygenation, free radicals, and stress granules. Cancer Cell. 2004; 5(5):429–41. [PubMed: 15144951]
11. Wen B, Burgman P, Zanzonico P, et al. A preclinical model for noninvasive imaging of hypoxia-induced gene expression; comparison with an exogenous marker of tumor hypoxia. Eur J Nucl Med Mol Imaging. 2004; 31(11):1530–8. [PubMed: 15378285]
12. Serganova I, Doubrovin M, Vider J, et al. Molecular imaging of temporal dynamics and spatial heterogeneity of hypoxia-inducible factor-1 signal transduction activity in tumors in living mice. Cancer Res. 2004; 64(17):6101–8. [PubMed: 15342393]
13. Alauddin MM, Conti PS, Fissekis JD. A general synthesis of [18F] labeled 2′-deoxy-2′-fluoro-1-β-D-arabinofuranosyluracil nucleosides. J Labelled Comp Radiopharm. 2003; 46:285–9.
14. Daldrup H, Shames DM, Wendland M, et al. Correlation of dynamic contrast-enhanced MR imaging with histologic tumor grade: comparison of macromolecular and small-molecular contrast media. AJR Am J Roentgenol. 1998; 171(4):941–9. [PubMed: 9762973]
15. Tofts PS. Modeling tracer kinetics in dynamic Gd-DTPA MR imaging. J Magn Reson Imaging. 1997; 7(1):91–101. [PubMed: 9039598]
16. Weissleder R, Cheng HC, Marecos E, Kwong K, Bogdanov A Jr. Non-invasive in vivo mapping of tumour vascular and interstitial volume fractions. Eur J Cancer. 1998; 34(9):1448–54. [PubMed: 9849430]
17. Wen X, Jackson EF, Price RE, et al. Synthesis and characterization of poly(L-glutamic acid) gadolinium chelate: a new biodegradable MRI contrast agent. Bioconjug Chem. 2004; 15(6): 1408–15. [PubMed: 15546209]
18. Maes F, Collignon A, Vandermeulen D, Marchal G, Suetens P. Multimodality image registration by maximization of mutual information. IEEE Trans Med Imaging. 1997; 16(2):187–98. [PubMed: 9101328]
19. Bidaut LM, Pascual-Marqui R, Delavelle J, et al. Three- to five-dimensional biomedical multisensor imaging for the assessment of neurological (dys) function. J Digit Imaging. 1996; 9(4):185–98. [PubMed: 8951098]
20. Nordsmark M, Alsner J, Keller J, et al. Hypoxia in human soft tissue sarcomas: adverse impact on survival and no association with p53 mutations. Br J Cancer. 2001; 84(8):1070–5. [PubMed: 11308256]
21. Hockel M, Schlenger K, Mitze M, Schaffer U, Vaupel P. Hypoxia and Radiation Response in Human Tumors. Semin Radiat Oncol. 1996; 6(1):3–9. [PubMed: 10717157]
22. Tatum JL, Kelloff GJ, Gillies RJ, et al. Hypoxia: importance in tumor biology, noninvasive measurement by imaging, and value of its measurement in the management of cancer therapy. Int J Radiat Biol. 2006; 82(10):699–757. [PubMed: 17118889]
23. Palcic B, Skarsgard LD. Reduced oxygen enhancement ratio at low doses of ionizing radiation. Radiat Res. 1984; 100(2):328–39. [PubMed: 6494444]
24. Hall, EJ.; Giaccia, AJ. Radiobiology for the Radiologist. 6th ed.. Lippincott Williams & Wilkins; Philadelphia, PA: 2004.
25. Pouyssegur J, Dayan F, Mazure NM. Hypoxia signalling in cancer and approaches to enforce tumour regression. Nature. 2006; 441(7092):437–43. [PubMed: 16724055]
26. Joyce JA. Therapeutic targeting of the tumor microenvironment. Cancer Cell. 2005; 7(6):513–20. [PubMed: 15950901]
27. Pugh CW, Ratcliffe PJ. Regulation of angiogenesis by hypoxia: role of the HIF system. Nat Med. 2003; 9(6):677–84. [PubMed: 12778166]
28. Kim WY, Oh SH, Woo JK, Hong WK, Lee HY. Targeting heat shock protein 90 overrides the resistance of lung cancer cells by blocking radiation-induced stabilization of hypoxia-inducible factor-1alpha. Cancer Res. 2009; 69(4):1624–32. [PubMed: 19176399]
29. Moeller BJ, Dreher MR, Rabbani ZN, et al. Pleiotropic effects of HIF-1 blockade on tumor radiosensitivity. Cancer Cell. 2005; 8(2):99–110. [PubMed: 16098463]
30. Jackson A, O'Connor JP, Parker GJ, Jayson GC. Imaging tumor vascular heterogeneity and angiogenesis using dynamic contrast-enhanced magnetic resonance imaging. Clin Cancer Res. 2007; 13(12):3449–59. [PubMed: 17575207]

31. Orth RC, Bankson J, Price R, Jackson EF. Comparison of single- and dual-tracer pharmacokinetic modeling of dynamic contrast-enhanced MRI data using low, medium, and high molecular weight contrast agents. Magn Reson Med. 2007; 58(4):705–16. [PubMed: 17899608]
32. Yankeelov TE, Niermann KJ, Huamani J, et al. Correlation between estimates of tumor perfusion from microbubble contrast-enhanced sonography and dynamic contrast-enhanced magnetic resonance imaging. J Ultrasound Med. 2006; 25(4):487–97. [PubMed: 16567438]
33. Niermann KJ, Fleischer AC, Huamani J, et al. Measuring tumor perfusion in control and treated murine tumors: correlation of microbubble contrast-enhanced sonography to dynamic contrast-enhanced magnetic resonance imaging and fluorodeoxyglucose positron emission tomography. J Ultrasound Med. 2007; 26(6):749–56. [PubMed: 17526606]
34. Fentzke RC, Korcarz CE, Lang RM, Lin H, Leiden JM. Dilated cardiomyopathy in transgenic mice expressing a dominant-negative CREB transcription factor in the heart. J Clin Invest. 1998; 101(11):2415–26. [PubMed: 9616213]
35. Mor-Avi V, Korcarz C, Fentzke RC, Lin H, Leiden JM, Lang RM. Quantitative evaluation of left ventricular function in a TransgenicMouse model of dilated cardiomyopathy with 2-dimensional contrast echocardiography. J Am Soc Echocardiogr. 1999; 12(3):209–14. [PubMed: 10070185]
36. Raman V, Artemov D, Pathak AP, et al. Characterizing vascular parameters in hypoxic regions: a combined magnetic resonance and optical imaging study of a human prostate cancer model. Cancer Res. 2006; 66(20):9929–36. [PubMed: 17047055]
37. Matsumoto S, Hyodo F, Subramanian S, et al. Low-field paramagnetic resonance imaging of tumor oxygenation and glycolytic activity in mice. J Clin Invest. 2008; 118(5):1965–73. [PubMed: 18431513]
38. Kung AL, Wang S, Klco JM, Kaelin WG, Livingston DM. Suppression of tumor growth through disruption of hypoxia-inducible transcription. Nat Med. 2000; 6(12):1335–40. [PubMed: 11100117]
39. Williams KJ, Telfer BA, Xenaki D, et al. Enhanced response to radiotherapy in tumours deficient in the function of hypoxia-inducible factor-1. Radiother Oncol. 2005; 75(1):89–98. [PubMed: 15878106]
40. Kioi M, Vogel H, Schultz G, Hoffman RM, Harsh GR, Brown JM. Inhibition of vasculogenesis, but not angiogenesis, prevents the recurrence of glioblastoma after irradiation in mice. J Clin Invest. 2010; 120(3):694–705. [PubMed: 20179352]
41. Powis G, Kirkpatrick L. Hypoxia inducible factor-1alpha as a cancer drug target. Mol Cancer Ther. 2004; 3(5):647–54. [PubMed: 15141023]
42. Belozerov VE, Van Meir EG. Hypoxia inducible factor-1: a novel target for cancer therapy. Anticancer Drugs. 2005; 16(9):901–9. [PubMed: 16162966]
43. Tang N, Wang L, Esko J, et al. Loss of HIF-1alpha in endothelial cells disrupts a hypoxia-driven VEGF autocrine loop necessary for tumorigenesis. Cancer cell. 2004; 6(5):485–95. [PubMed: 15542432]
44. Ryan HE, Poloni M, McNulty W, et al. Hypoxia-inducible factor-1alpha is a positive factor in solid tumor growth. Cancer Res. 2000; 60(15):4010–5. [PubMed: 10945599]
45. Blouw B, Song H, Tihan T, et al. The hypoxic response of tumors is dependent on their microenvironment. Cancer Cell. 2003; 4(2):133–46. [PubMed: 12957288]
46. Wenger RH. Cellular adaptation to hypoxia: O2-sensing protein hydroxylases, hypoxia-inducible transcription factors, and O2-regulated gene expression. Faseb J. 2002; 16(10):1151–62. [PubMed: 12153983]
47. Wang V, Davis DA, Haque M, Huang LE, Yarchoan R. Differential gene up-regulation by hypoxia-inducible factor-1alpha and hypoxia-inducible factor-2alpha in HEK293T cells. Cancer research. 2005; 65(8):3299–306. [PubMed: 15833863]

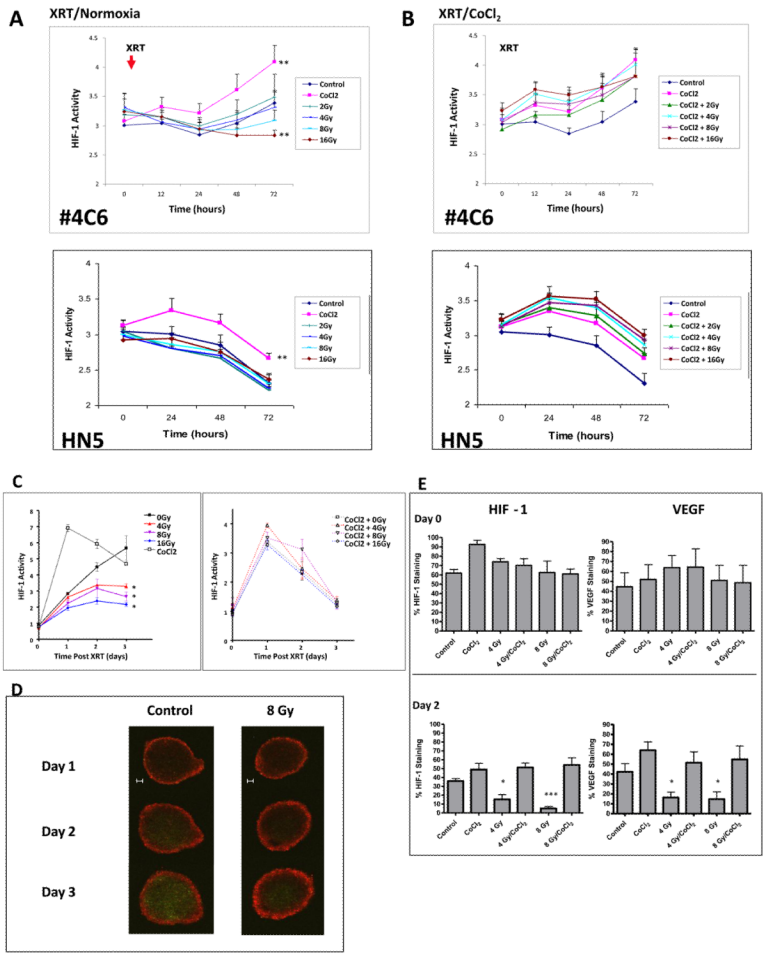

Figure 1.

A) Radiation inhibits HIF-1 signaling in aerobic #4C6 and HN5 monolayer cultures in a dose dependent fashion, but does not impact HIF-1 signaling in hypoxic monolayers. HIF-1 activity (GFP signal normalized to constitutive RFP signal, reported as mean values +/− s.d.) over time following radiation (timing of treatment designated "X") in normoxic and $CoCl_2$ treated (timing of treatment designated "C") monolayers. B) normalized HIF-1 signal at 72 hours post-irradiation in normoxic and hypoxic monolayers plotted against radiation dose. C) Radiation inhibits initial development of, but not pre-established, hypoxia signaling within #4C6 spheroid cultures. HIF-1 dependent GFP signal normalized to constitutive RFP signal, reported as mean values +/− s.d. All statistical comparisons are with controls at identical timepoints; *, $p < 0.05$. D) Serial fluorescence photomicrographs of representative spheroids over time, at designated timepoints. Bar = 100 μm. E) Spheroids were treated with 0, 4 or 8 Gy single fraction radiation 2 days after plating, +/− concurrent 200 μM CoCl2. Immunohistochemical staining results for HIF-1 and VEGF expression for each treatment condition were pooled (approximately 30 images total) and reported as mean % staining of total tissue area +/− s.d. All statistical comparisons are with baseline controls at designated timepoints; *, $p < 0.05$; ***, $p < 0.001$.

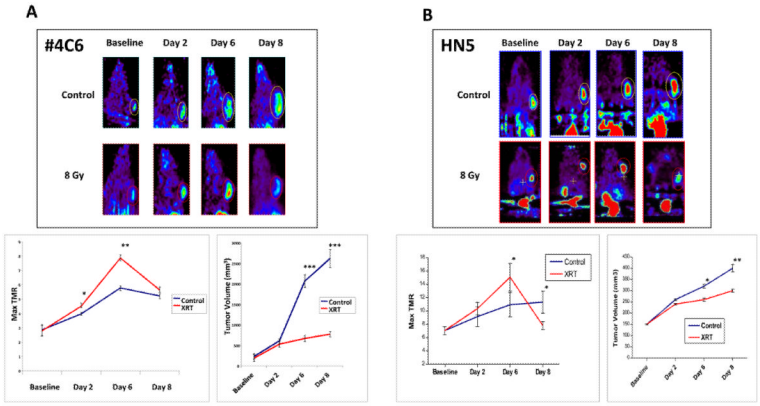

Figure 2.

Radiation induces delayed HIF-1 signaling in A) #4C6 and B) HN5 xenografts. Top: whole animal ^{18}F-FEAU PET imaging, with tumors indicated by ovals. Bottom left: pooled quantification of ^{18}F-FEAU tumor-muscle signal ratio (TMR; *, $p < 0.05$ between treatment groups; **, $p < 0.005$ between treatment groups). Bottom right: volumetric tumor growth over time, reported as mean tumor volume values +/− standard error; ***, $p < 0.001$.

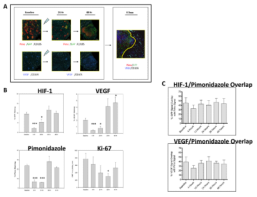

Figure 3.

Post-radiation *in vivo* HIF-1 signal induction results from stromal vessel dysfunction and ischemic insult. A) Serial 4X photomicrographs of immunohistochemical staining for HIF-1, pimonidazole, VEGF, and CD105+ microvessels in control and irradiated #4C6 xenograft tumors. Images from 24 hours post-treatment tissue samples illustrate focal radioresistant HIF-1 dependent GFP signal and VEGF expression in regions retaining pimonidazole 24 hours post-treatment. By 8 days post-treatment, normalization of HIF-1 transcriptional activity, VEGF expression, and pimonidazole staining is seen in revascularized regions populated with CD105+ vessels. However, tumor adaptation is not uniform; areas of pimonidazole retention, HIF-1 dependent GFP signal, and VEGF protein co-localize to focal devascularized regions (to the left of the revascularized region demarcated by the solid yellow line), recapitulating the heterogeneous tumor microenvironment seen at baseline. B) Quantification of % staining of total tissue area over time in pooled tissue sections, reported as mean values +/− s.d. All statistical comparisons are with baseline pretreatment values; *, $p < 0.05$; ***, $p < 0.001$. C) Quantified pixel-by-pixel analysis of % spatial overlap +/− s.d. between GFP/VEGF signal and pimonidazole, at baseline and following irradiation.

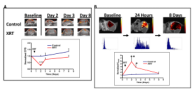

Figure 4.

A) Serial color power Doppler imaging of a representative #4C6 xenograft demonstrates transient loss of central and peripheral tumor vascular flow by 24 hours post-radiation, followed by early stromal vessel recovery 48 hours post-treatment. Statistical comparisons of pooled results at each posttreatment timepoint are with baseline pretreatment values; ***, $p < 0.001$. B) Serial single-tracer DCE-MRI mapping of volume transfer constant (K^{trans}) values in a representative #4C6 xenograft demonstrates increased K^{trans} values by 24 hours post-radiation, consistent with loss of vascular integrity. Corresponding K^{trans} value distribution histograms are shown below each image. K^{trans} values normalize towards baseline values by 7 days post-treatment. Statistical comparisons of pooled results at each timepoint are with baseline findings, as reported as mean values +/− s.d; *, $p < 0.05$; **, $p < 0.005$.

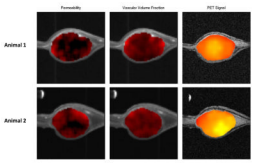

Figure 5.
Dual-tracer DCE-MRI parametric maps of vascular function co-registered with HIF-1-specific PET imaging of an immobilized dorsal skin window C6#4 reporter tumor model 48 hours following 8 Gy treatment. Columns demonstrate, from left-to-right, 1) low molecular weight contrast-dependent permeability mapping, 2) high molecular weight PG-Gd-DTPA contrast-dependent vascular volume fraction mapping, and 3) HIF-1 dependent ^{18}F-FEAU retention imaged at mid-plane within two representative tumors (top and bottom rows), with regions of impaired microvessel low molecular weight tracer delivery to the extravascular compartment spatially corresponding with regions of elevated HIF-1 dependent signal.

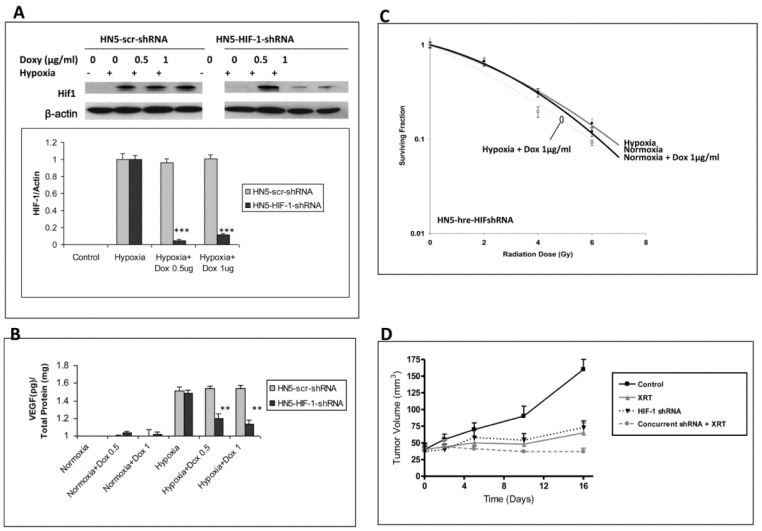

Figure 6.

In vitro conditional knockdown of HIF-1 and downstream soluble VEGF expression in response to moderate hypoxia was measured by A) Western blot and B) ELISA assays, respectively, in HN5-HIF-1-shRNA cells treated with doxycycline at 0, 0.5, or 1 ug/ml in normoxic conditions in serum-starved (1% FBS) media for 48 hours, then transferred to 1% O2 for 24 hours with constant doxycycline concentration before collection; **, $p < 0.005$; ***, $p < 0.001$. HN5-scr-shRNA = scrambled shRNA controls. C) *In vitro* HN5-HIF-1-shRNA clonogenic survival curves. D) *In vivo* HN5-HIF-1-shRNA xenograft tumor growth.